Proceedings of the ASME 2014 International Mechanical Engineering Congress & Exposition
IMECE2014
November 14-20, 2014, Montreal, Quebec, Canada

IMECE2014-40124

THE EFFECT OF NONCONDENSABLES ON THE BUOYANCY-THERMOCAPILLARY CONVECTION IN CONFINED AND VOLATILE FLUIDS

Tongran Qin
George W. Woodruff School
of Mechanical Engineering
Georgia Institute of Technology
Atlanta, GA 30332-0405, USA
Email: tongran@gatech.edu

Minami Yoda
George W. Woodruff School
of Mechanical Engineering
Georgia Institute of Technology
Atlanta, GA 30332-0405, USA
Email: minami@gatech.edu

Roman O. Grigoriev
School of Physics
Georgia Institute of Technology
Atlanta, GA 30332-0430, USA
Email: romgrig@gatech.edu

ABSTRACT

Convection in confined layers of volatile liquids has been studied extensively under atmospheric conditions. Recent experimental results [1] have shown that removing most of the air from a sealed cavity significantly alters the flow structure and, in particular, suppresses transitions between the different convection patterns found at atmospheric conditions. Yet, at the same time, this has almost no effect on the flow speeds in the liquid layer. To understand these results, we have formulated and numerically implemented a detailed transport model that accounts for mass and heat transport in both phases as well as the phase change at the interface. Surprisingly, the numerical simulations show that noncondensables have a large effect on buoyancy-thermocapillary flow at concentrations even as low as 1%, i.e., much lower than those achieved in experiment.

INTRODUCTION

Convection in a layer of fluid with a free surface due to a combination of thermocapillary stresses and buoyancy has been studied extensively due to applications in thermal management in terrestrial environments. In particular, devices such as heat pipes and heat spreaders, which use phase change to enhance thermal transport, are typically sealed, with noncondensables (such as air), which can impede phase change, removed [2]. However, air tends to dissolve in liquids and be adsorbed into solids, so removing it completely is practically impossible. Hence, the liquid film almost always remains in contact with a mixture of its own vapor and some air.

The fundamental studies on which the design of such devices is based, however, often do not distinguish between different compositions of the gas phase. The experimental studies are in many cases performed in geometries that are not sealed and hence contain air at atmospheric pressure, while most theoretical studies ignore phase change completely. Those that do consider phase change use transport models of the gas phase that are limited, and hence do not properly describe the effect of noncondensables on the flow in the liquid layer. Yet, as a recent experimental study by Li *et al.* [1] shows, noncondensables can play an important and nontrivial role, so the results in one limit cannot be simply extrapolated to the other.

Most of the existing analytical and numerical studies use one-sided models which describe transport in the liquid, but not the gas, phase and ignore phase change, with both phase change and transport in the gas phase indirectly incorporated through boundary conditions at the liquid-vapor interface. We have recently introduced a comprehensive two-sided model [3] of buoyancy-thermocapillary convection in confined fluids which provides a detailed description of momentum, heat and mass transport in both the liquid and the gas phase as well as phase change at the interface. In the limit where the system is at ambient (atmospheric) conditions, this model shows that convection patterns are not described by the theory developed for the dynamic Bond number $Bo_D = 0$ limit, even though thermocapillarity still dominates buoyancy for Bond numbers of order unity [4, 5]. Instead the flow in the liquid layer transitions from

a steady unicellular pattern (featuring a single large convection roll) to a steady multicellular pattern (featuring multiple steady convection rolls) to an oscillatory pattern (featuring multiple unsteady convection rolls) as the applied temperature gradient is increased, which is consistent with previous experimental studies of volatile and nonvolatile fluids [1, 6–9], as well as previous numerical studies of nonvolatile fluids [6, 10–13]. These results justify the use of one-sided models in the limit where the gas phase is dominated by noncondensables (and hence phase change is strongly suppressed).

In comparison, very few studies have been performed in the (near) absence of noncondensables. In particular, the theoretical studies [14–18] employ extremely restrictive assumptions and/or use a very crude description of one of the two phases. A variation of our two-sided model [19] predicts that the interfacial temperature becomes essentially constant in the absence of noncondensables, so that thermocapillarity is negligible and the flow is primarily driven by buoyancy, which leads to significant changes in the structure of the base flow. Furthermore, the model predicts that there is only steady unicellular flow, and that there should be no transitions to multiple steady or unsteady rolls in this limit as the applied temperature difference increases.

The latter prediction was confirmed by Li *et al.* [1], who performed experiments for a volatile silicone oil at $Bo_D = O(1)$. They found that the transitions between different convection patterns are suppressed when the concentration of noncondesables is reduced, and observed only the steady unicellular regime over the entire range of imposed temperature gradients at their lowest average air concentration (11%). Interestingly, the experiments also show that at small imposed temperature gradients the flow structure and speeds remain essentially the same as the air concentration decreases from 96% (ambient conditions) to 11%. Since we know that the flow is dominated by buoyancy in the absence of air, these observations suggest that thermocapillarity is still dominant, and that the flow must change from one dominated by thermocapillarity to one dominated by buoyancy at even lower air concentrations.

To better understand the effect of noncondensables on heat and mass transport in volatile fluids in confined and sealed geometries, our two-sided model [**?**, 3, 19] was further generalized to describe situations where the gas phase is dominated by vapor, but still contains a small amount of air [**?**]. The model is described in detail, and the results of the numerical investigations of this model are presented, analyzed, and compared with experimental observations below.

MATHEMATICAL MODEL

Governing Equations

We describe transport in both the liquid and the gas phase using a generalization of the model described in [19]. Both phases are considered incompressible and the momentum transport in the bulk is described by the Navier-Stokes equation

$$\rho\left(\partial_t \mathbf{u} + \mathbf{u}\cdot\nabla\mathbf{u}\right) = -\nabla p + \mu\nabla^2\mathbf{u} + \rho\left(T\right)\mathbf{g} \tag{1}$$

where p is the fluid pressure, ρ and μ are the fluid's density and viscosity, respectively, and $\mathbf{g}$ is the gravitational acceleration.

Following standard practice, we use the Boussinesq approximation, retaining the temperature dependence only in the last term to represent the buoyancy force. In the liquid phase

$$\rho_l = \rho_l^*[1 - \beta_l\left(T - T^*\right)], \tag{2}$$

where ρ_l^* is the reference density at the reference temperature T^* and $\beta_l = -(\partial\rho_l/\partial T)/\rho_l$ is the coefficient of thermal expansion. Here and below, subscripts l, g, v, a and i denote properties of the liquid and gas phase, vapor and air component, and the liquid-gas interface, respectively. In the gas phase

$$\rho_g = \rho_a + \rho_v, \tag{3}$$

where both vapor ($n = v$) and air ($n = a$) are considered to be ideal gases

$$p_n = \rho_n \bar{R}_n T, \tag{4}$$

$\bar{R}_n = R/M_n$, R is the universal gas constant, and M_n is the molar mass. The total gas pressure is the sum of partial pressures

$$p_g = p_a + p_v. \tag{5}$$

On the left-hand-side of (1) the density is considered constant for each phase (defined as the spatial average of $\rho(T)$).

Due to the lack of a computationally tractable generalization of the Navier-Stokes equation for multi-component mixtures, the model is restricted to situations where the dilute approximation is valid in the gas phase, *e.g.* when the molar fraction of one component is much greater than that of the other.

For a volatile fluid in confined geometry, the external temperature gradient causes both evaporation and condensation, with the net mass of the fluid being globally conserved. Conventionally, the mass transport of the less abundant component is described by the advection-diffusion equations for its concentration (defined as the molar fraction). To ensure local mass conservation, we use the advection-diffusion equation for the density of the less abundant component instead. Since the case when air dominates was treated in Ref. [3], we only describe here the case when vapor dominates, in which case

$$\partial_t \rho_a + \mathbf{u}\cdot\nabla\rho_a = D\nabla^2\rho_a, \tag{6}$$

where D is the binary diffusion coefficient of one component in the other. Mass conservation for liquid and its vapor requires

$$\int_{\text{liquid}} \rho_l dV + \int_{\text{gas}} \rho_v dV = m_{l+v}, \tag{7}$$

where m_{l+v} is the total mass of liquid and vapor. The total pressure in the gas phase is $p_g = p + p_o$, where the pressure offset p_o is

$$p_o = \left[\int_{\text{gas}} \frac{1}{\bar{R}_v T} dV\right]^{-1} \left[m_{l+v} - \int_{\text{liquid}} \rho_l dV - \int_{\text{gas}} \frac{p}{\bar{R}_v T} dV\right]. \tag{8}$$

The concentration of the two components can be computed from the equation of state using the partial pressure

$$c_n = p_n / p_g. \tag{9}$$

Finally, the transport of heat is also described using an advection-diffusion equation

$$\partial_t T + \mathbf{u} \cdot \nabla T = \alpha \nabla^2 T, \tag{10}$$

where $\alpha = k/(\rho c_p)$ is the thermal diffusivity, k is the thermal conductivity, and c_p is the heat capacity, of the fluid.

Boundary Conditions

The system of coupled evolution equations for the velocity, pressure, temperature, and density fields has to be solved in a self-consistent manner, subject to the boundary conditions describing the balance of momentum, heat, and mass fluxes. The phase change at the liquid-gas interface can be described using Kinetic Theory [20]. The mass flux across the interface is given by [21]

$$J = \frac{2\lambda}{2-\lambda} \rho_v \sqrt{\frac{\bar{R}_v T_i}{2\pi}} \left[\frac{p_l - p_g}{\rho_l \bar{R}_v T_i} + \frac{\mathscr{L}}{\bar{R}_v T_i} \frac{T_i - T_s}{T_s}\right], \tag{11}$$

where λ is the accommodation coefficient, which is usually taken to be equal to unity (the convention we follow here), and subscript s denotes saturation values for the vapor. The dependence of the local saturation temperature on the partial pressure of vapor is described using the Antoine equation for phase equilibrium

$$\ln p_v = A_v - \frac{B_v}{C_v + T_s} \tag{12}$$

where A_v, B_v, and C_v are empirical coefficients.

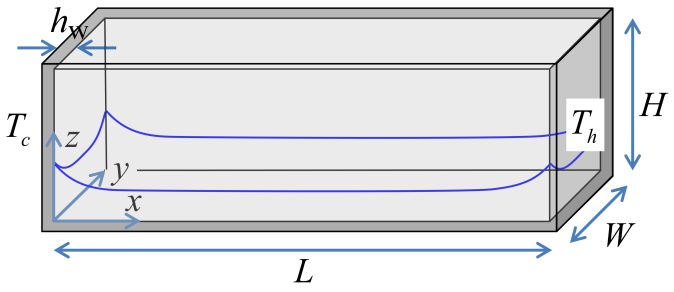

FIGURE 1. The test cell containing the liquid and air/vapor mixture. Gravity is pointing in the negative z direction. The shape of the contact line reflects the curvature of the free surface.

The mass flux balance on the gas side of the interface is given by

$$J = -D\mathbf{n} \cdot \nabla \rho_v + \rho_v \mathbf{n} \cdot (\mathbf{u}_g - \mathbf{u}_i), \tag{13}$$

where the first term represents the diffusion component, and the second term represents the advection component (referred to as the "convection component" by Wang *et al.* [22]) and $\mathbf{u}_i$ is the velocity of the interface. Since air is noncondensable, its mass flux across the interface is zero:

$$0 = -D\mathbf{n} \cdot \nabla \rho_a + \rho_a \mathbf{n} \cdot (\mathbf{u}_g - \mathbf{u}_i). \tag{14}$$

For binary diffusion, the diffusion coefficient of vapor in air is the same as that of air in vapor, while the concentration gradients of vapor and air have the same absolute value but opposite directions, which yields the relation between the density gradients of vapor and air

$$\frac{\mathbf{n} \cdot \nabla \rho_v}{M_v} + \frac{\mathbf{n} \cdot \nabla \rho_a}{M_a} = -\frac{p_g}{R T_i^2} (\mathbf{n} \cdot \nabla T_g), \tag{15}$$

Finally, the heat flux balance is given by

$$\mathscr{L} J = \mathbf{n} \cdot k_g \nabla T_g - \mathbf{n} \cdot k_l \nabla T_l. \tag{16}$$

The remaining boundary conditions for $\mathbf{u}$ and T at the liquid-vapor interface are standard: the temperature is considered to be continuous

$$T_l = T_i = T_v \tag{17}$$

as are the tangential velocity components

$$(1 - \mathbf{n} \cdot \mathbf{n})(\mathbf{u}_l - \mathbf{u}_g) = 0. \tag{18}$$

The normal component of $\mathbf{u}_l$ is computed using mass balance across the interface. Furthermore, since the liquid density is much greater than that of the gas,

$$\mathbf{n}\cdot(\mathbf{u}_l-\mathbf{u}_i)=\frac{J}{\rho_l}\approx 0. \tag{19}$$

The stress balance

$$(\Sigma_l-\Sigma_g)\cdot\mathbf{n}=\mathbf{n}\kappa\sigma-\gamma\nabla_s T_i \tag{20}$$

incorporates both the viscous drag between the two phases and thermocapillary effects. Here $\Sigma=\mu\left[\nabla\mathbf{u}-(\nabla\mathbf{u})^T\right]-p$ is the stress tensor, κ is the interfacial curvature, $\nabla_s=(1-\mathbf{n}\cdot\mathbf{n})\nabla$ is the surface gradient and $\gamma=-\partial\sigma/\partial T$ is the temperature coefficient of surface tension.

Newton's iteration is used to solve for the mass flux J, the interfacial temperature T_i, the saturation temperature T_s, the normal component of the gas velocity at the interface $\mathbf{n}\cdot\mathbf{u}_g$, the density of the dominant component in the gas phase and the normal component of the density gradient of the less abundant component on the gas side (respectively vapor and air, except at atmospheric conditions).

We further assume that the fluid is contained in a rectangular test cell with inner dimensions $L\times W\times H$ (see Figure 1) and thin walls of thickness h_w and conductivity k_w. The left wall is cooled with constant temperature T_c imposed on the outside, while the right wall is heated with constant temperature $T_h>T_c$ imposed on the outside. Since the walls are thin, one-dimensional conduction is assumed, yielding the following boundary conditions on the inside of the side walls:

$$T|_{x=0}=T_c+\frac{k_n}{k_w}h_w\,\mathbf{n}\cdot\nabla T, \tag{21}$$

$$T|_{x=L}=T_h+\frac{k_n}{k_w}h_w\,\mathbf{n}\cdot\nabla T, \tag{22}$$

where $n=g$ ($n=l$) above (below) the contact line.

Heat flux through the top, bottom, front and back walls is ignored (which is usually the case in most experiments). Standard no-slip boundary conditions $\mathbf{u}=0$ for the velocity and no-flux boundary conditions

$$\mathbf{n}\cdot\nabla\rho_n=0 \tag{23}$$

for the density of the less abundant component ($n=a$ or, at atmospheric conditions, $n=v$), are imposed on all the walls. The pressure boundary condition

$$\mathbf{n}\cdot\nabla p=\rho(T)\,\mathbf{n}\cdot\mathbf{g} \tag{24}$$

follows from (1).

RESULTS AND DISCUSSION

The model described above has been implemented numerically by adapting an open-source general-purpose CFD package OpenFOAM [23] to solve the governing equations in both 2D and 3D geometries. Details are available in Ref. [3].

The computational model was used to investigate the buoyancy-thermocapillary flow of a fluid confined in a sealed rectangular test cell with dimensions identical to that used in the experimental study of Li *et al.* [1]. The working fluid is hexamethyldisiloxane, a silicone oil with a kinematic viscosity $\nu=0.65$ cSt, which is a volatile liquid with the properties summarized in Table 1. A layer of liquid of average thickness $d_l=2.5$ mm is confined and sealed in the test cell with the inner dimensions $L\times H\times W=48.5$ mm $\times 10$ mm $\times 10$ mm (see Figure 1), below a layer of gas, which is a mixture of vapor and air. The pressures in the test cell ranged from the vapor pressure (0% air) to atmospheric (96% air). The walls of the test cell are made of quartz (fused silica) with thermal conductivity $k_w=1.4$ W/m-K and have thickness $h_w=1.25$ mm. Silicone oil wets quartz very well, but in the numerics we set the contact angle $\theta=50^\circ$ (unless noted otherwise) to avoid numerical instabilities. This has a minor effect on the shape of the free surface everywhere except very near the contact lines; moreover, previous studies [3] over a relatively large range of contact angles show that it has a minor influence on the flow pattern.

While the numerical model can describe the flows in both 2D and 3D systems, the results presented here are obtained for 2D flows (ignoring variation in the y-direction), since 3D simulations require significant computational resources and comparison of 2D and 3D results for the same system under air at atmospheric conditions showed that 3D effects are relatively weak [3]. The 2D system corresponds to the central vertical (x-z) plane of the test cell.

Initially, it is assumed that the fluid is stationary with uniform temperature $T_0=(T_c+T_h)/2$ (we set $T_0=293$ K in all cases), the liquid layer is of uniform thickness (such that the liquid-gas interface is flat), and the gas layer is a uniform mixture of the vapor and the air. The partial pressure of the vapor $p_v=p_s(T_0)$ is set equal to the saturation pressure at T_0, $p_s(T_0)\approx 4.1$ kPa, calculated from (12). The partial pressure of air p_a was used as a control parameter, which determines the net mass of air in the cavity. Constant (*vs.* temperature-dependent) properties were used in these simulations (although incorporating this dependence is straightforward) because initial simulations showed that the variations in the fluid properties due to temperature had a negligible effect on the heat and mass transport.

As the system evolves towards an asymptotic state, the flow develops in both phases, the interface distorts to accommodate the assigned contact angle at the walls, and the gradients in the

	liquid	vapor	air
μ (kg/(m·s))	5.27×10^{-4}	5.84×10^{-6}	1.81×10^{-5}
ρ (kg/m^3)	765.5	0.27	1.20
β (1/K)	1.32×10^{-3}	3.41×10^{-3}	3.41×10^{-3}
k (W/(m·K))	0.110	0.011	0.026
α (m^2/s)	7.49×10^{-8}	2.80×10^{-5}	2.12×10^{-5}
Pr	9.19	0.77	0.71
D (m^2/s)	-	1.46×10^{-4}	5.84×10^{-6}
σ (N/m)	1.58×10^{-2}		
γ (N/(m·K))	8.9×10^{-5}		
$\mathscr{L}$ (J/kg)	2.25×10^5		

TABLE 1. Material properties of pure components at the reference temperature $T_0 = 293$ K [?, ?]. The properties of the gas phase are taken equal to those of the dominant component.

temperature and vapor concentration are established. The simulations are first performed on a coarse hexahedral mesh (initially all cells are cubic with a dimension of 0.5 mm), since the initial transient state is of secondary interest. Once the transient dynamics have died down, the simulations are continued after the mesh is refined in several steps, until the results become mesh-independent.

Fluid Flow and Temperature Fields

In order to investigate the effect of noncondensables on the the flow, we performed numerical simulations at a fixed temperature difference $\Delta T = 10$ K, with the average concentration of air $\bar{c}_a$ varying between 0% (pure vapor) and 96% (atmospheric pressure). After an initial transient, the flow reaches steady state. Figure 2 shows the streamlines of this steady flow in both the liquid and the gas phases.

The concentration of noncondensables has a significant impact on the flow in both layers. In the absence of air, the flow in the liquid is dominated by two counterclockwise convection rolls, a larger one near the cold wall and a smaller one near the hot wall. At $\bar{c}_a = 0.16$ (16% air), the flow in the liquid in the central region of the cell is best described as a horizontal return flow with two convection rolls localized near the hot and the cold end. When the system is at atmospheric pressure (when the air dominates the gas phase with $\bar{c}_a = 0.96$), multiple convections rolls emerge, covering the entire liquid layer. In this case the flow pattern can be classified as steady multicellular flow (SMC) and thermocapillarity is the dominant driving force [3]. These results are consistent with the experimental findings of Li *et al.* [1]

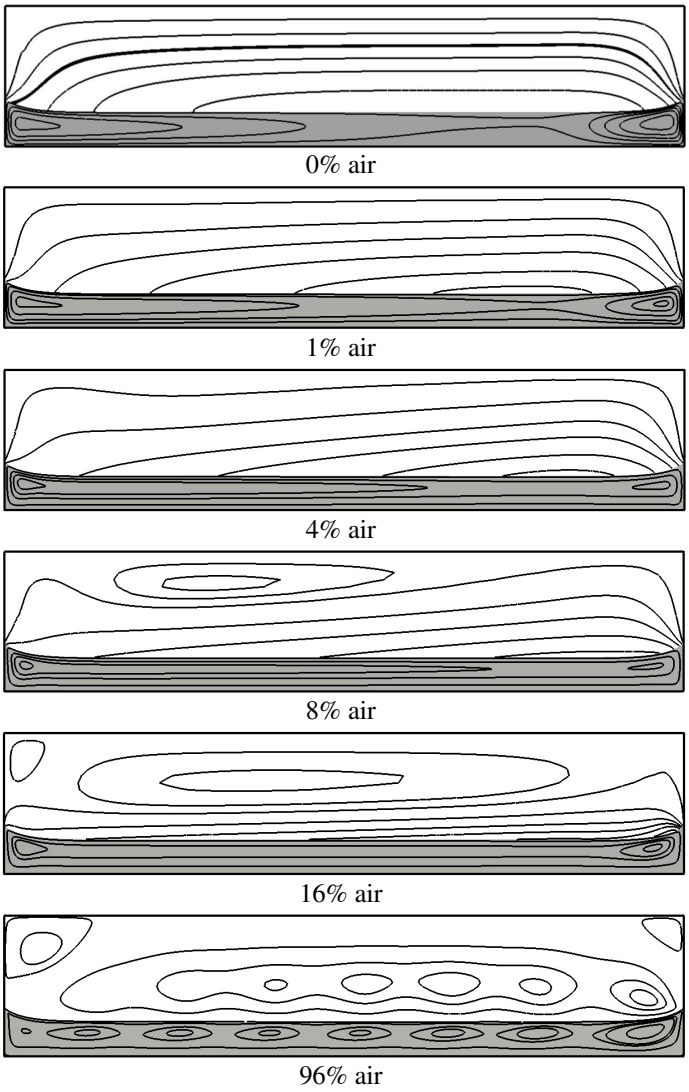

FIGURE 2. Streamlines of the flow (solid lines) at different average concentrations of air. The temperature difference is $\Delta T = 10$ K. Here and below, the gray (white) background indicates the liquid (gas) phase.

who find that multicellular convection pattern disappears and is replaced with unicellular flow in the liquid layer when the concentration of noncondensables is reduced (at a fixed ΔT) from 96% to 11%.

The flows in the gas phase are also qualitatively different. In the absence of air, the flow in the gas phase is unidirectional, with the liquid evaporating near the hot wall, the resultant vapor flowing from the hot wall to the cold wall, and then condensing there. Noncondensable gases suppress the phase change, since the vapor need to diffuse away from (or towards) the interface as it evaporates (or condenses). Furthermore, since air cannot condense, its presence also alters the flow pattern in the gas phase. However, when the concentration of air is relatively small (less

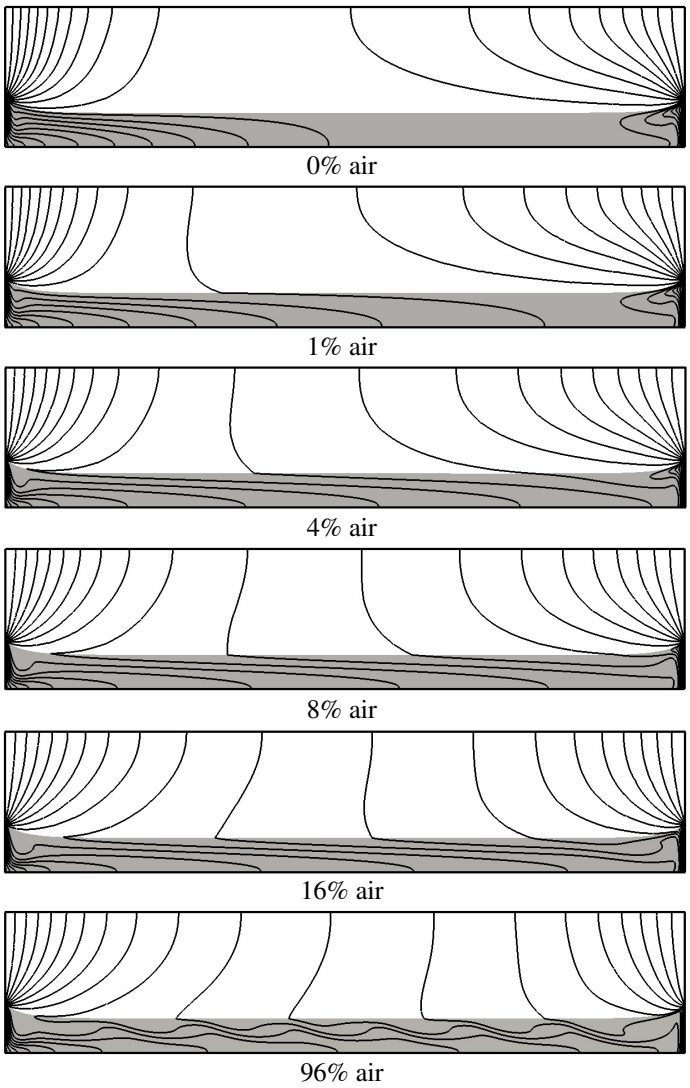

FIGURE 3. The temperature field inside the cell at different average concentrations of air. The temperature difference is $\Delta T = 10$ K and the difference between adjacent isotherms (solid lines) is 0.5 K.

than about 4%), the flow of the air-vapor mixture remains essentially unidirectional.

A (clockwise) recirculation roll emerges in the central region near the top wall at around $\bar{c}_a = 0.08$ and expands as $\bar{c}_a$ increases. Additional (counterclockwise) recirculation rolls emerge in the top corners at around $\bar{c}_a = 0.16$. The clockwise rolls must be driven by thermocapillarity, which pulls the vapor above the interface to the cold end wall, while the counterclockwise rolls are driven by buoyancy. At atmospheric pressure ($\bar{c}_a = 0.96$), a number of small (clockwise) recirculation rolls develop in the gas phase directly above the recirculation rolls in the liquid phase. They are driven by thermocapillarity as opposed to the (counterclockwise) rolls in the top corners that are driven by buoyancy.

Figure 3 shows the temperature fields corresponding to the flows shown in Figure 2. In the absence of air, the isotherms are clustered near the hot and cold end walls, indicating the formation of sharp thermal boundary layers near both end walls, with the temperature being essentially constant along almost the entire liquid-gas interface. As the concentration of air increases, the thermal boundary layers expand and the temperature gradient gradually becomes more uniform. At atmospheric pressure the isotherms become wavy in the liquid phase, reflecting the convective motion of the fluid.

While buoyancy is mainly controlled by the temperature of the fluid near the end walls, which is mostly unaffected by the presence of noncondensables, thermocapillarity is controlled by the temperature of the fluid at the interface, which varies significantly with $\bar{c}_a$. We investigate this dependence in more detail in the next section.

Interfacial Temperature

The variation of the interfacial temperature T_i along the interface (relative to its spatial average $\langle T_i \rangle_x \approx T_0$) is shown in Figure 4. At atmospheric pressure, when air dominates, T_i varies nearly linearly along almost the entire interface, with the modulation corresponding to the advection of heat by convective flow. The average of the interfacial temperature gradient $\tau = \partial T_i / \partial x$ is comparable to the value of the imposed temperature gradient $\Delta T / L$. As the concentration of air decreases, τ also decreases. When $\bar{c}_a$ is reduced to around 1%, T_i starts to deviate from the linear profile, with τ near the hot end wall decreasing more than near the cold end wall. In the complete absence of air, the interfacial temperature becomes essentially constant. The value of τ decreases by three orders of magnitude, compared with the values found under air at the same ΔT [19], and the thermocapillary stresses become negligible.

Numerical simulations show that there is a high degree of correlation between the spatial profiles of T_i and p_v. As Figure 5 illustrates, p_v also varies linearly with x over almost the entire interface. Since

$$\delta p_v = p_v - \langle p_v \rangle_x = p_g (c_v - \bar{c}_v) = -p_g (c_a - \bar{c}_a) \qquad (25)$$

and $p_g \approx (1 - \bar{c}_a)^{-1} p_v(T_0)$ is constant in the gas phase, this result implies that the gradient of the concentration $\zeta = \partial_x c_a = -p_g \partial_x p_v$ is independent of x in the core region of the flow for all $\bar{c}_a$ above 1%. For concentrations of order 1% and below, the strong vapor flow from the hot to the cold wall sweeps the air away from the hot end wall, further depleting the concentration gradient there, which leads to the predicted asymmetry in the gradients of both c_a and p_v.

The relationship between the two gradients can be obtained by a straightforward analysis of the theoretical model. Using (11)

the interfacial temperature can be written as

$$T_i \approx T_s + \underbrace{\frac{2-\lambda}{2\lambda}\sqrt{\frac{2\pi}{\bar{R}_v T_s}}\frac{\bar{R}_v T_s^2}{\rho_v \mathscr{L}} J}_{T_p} - \underbrace{\frac{T_s}{\rho_l \mathscr{L}}(p_l - p_v)}_{T_c}. \quad (26)$$

The three terms on the right-hand side describe the effects of variation in the saturation pressure, phase change, and interfacial curvature, respectively. The dominant physical effect is different in the two limiting cases considered ($\bar{c}_a = 0$ and $\bar{c}_a \approx 1$). Detailed analysis in Ref. [19] shows that at ambient conditions with air dominant in the gas phase, T_c and T_p are negligible compared to the variation in T_s. Hence the value of the interfacial temperature gradient τ is determined by the variation of the saturation temperature which, in turn, is mostly a function of the local concentration c_a. This will still be the case as long as the variation in the concentration of air is non-negligible, that is for $\bar{c}_a$ values that exceed a fraction of a percent. In the complete absence of air ($\bar{c}_a = 0$), the variation in T_s becomes negligible and the variation in T_i is mainly due to the latent heat released or absorbed at the interface, which is described by T_p. The variation in ΔT_p in this limit is almost four orders of magnitude smaller than the imposed temperature difference ΔT, so the interface can effectively be considered isothermal.

The quantitative relation between τ and ζ can be found from the Clausius-Clapeyron equation, which is equivalent to (12) for moderate ΔT, with the help of (4) and (9):

$$\tau = \nabla T_s = \frac{\partial T_s}{\partial p_v}\nabla p_v \approx \frac{\bar{R}_v T_0^2}{\mathscr{L} p_v} p_g \nabla c_v = -\frac{\bar{R}_v T_0^2}{\mathscr{L}}\frac{1}{1-\bar{c}_a}\zeta, \quad (27)$$

where p_v is taken at the reference temperature T_0 and so can be considered constant. Eq. (27) shows the interfacial temperature is controlled completely by the composition of (or mass transport in) the gas phase.

Note that this relationship is expected to hold with very good precision in the entire range of $\bar{c}_a$. This is indeed what we find by comparing the results shown in Figures 4 and 5. In particular, when the vapor dominates, $\bar{c}_a \ll 1$ and $p_g \approx p_v$. Substituting the fluid properties from Table 1 into (27) we find $\tau \approx (-20\text{ K})\zeta$, which is in good agreement with the numerical results.

Interfacial Velocity

As we have pointed out, the velocity field in the liquid is expected to be substantially different in the two limits. Indeed, in the limit $\bar{c}_a \to 0$, the interfacial temperature gradient τ essentially disappears, so thermocapillary stresses, which dominates the flow at ambient conditions ($\bar{c}_a \approx 1$), vanish. As we have shown in Ref. [19], the ratio of the characteristic velocity at the free surface due to thermocapillarity (u_T) and due to buoyancy (u_B) is $u_T/u_B = 12L\tau/\Delta T Bo_D^{-1}$. In the experiments of Li *et al.* [1] $Bo_D \approx 0.7$, so thermocapillarity is expected to dominate the flow when $\tau > 0.06\Delta T/L$. As Figure 4 illustrates, this conditions is clearly satisfied along the entire free surface for $\bar{c}_a \gtrsim 0.04$. This can be seen more clearly in Figure 6 which shows the flow velocity u_i at the interface for different average concentrations of air.

The flow is predicted to be the fastest at ambient conditions because (average) τ is the largest, and hence the thermocapillary stresses are the strongest, at $\bar{c}_a = 0.96$, according to Figure 4. Periodic oscillations in T_i are reflected in the periodic variation in the temperature gradient τ, and hence the flow velocity u_i in the core region. As $\bar{c}_a$ decreases, the interfacial velocity is predicted to decreases as well, however, the flow in the core region at both $\bar{c}_a = 0.16$ and $\bar{c}_a = 0.08$ is found to be only slightly slower

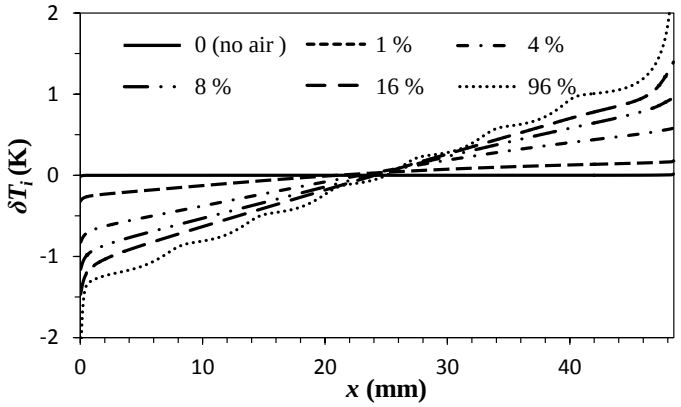

FIGURE 4. Interfacial temperature profile for different average concentrations of air and $\Delta T = 10$ K. To amplify the variation of T_i in the central region of the cell we plotted the variation $\delta T_i = T_i - \langle T_i \rangle_x$ about the average and truncated the y-axis.

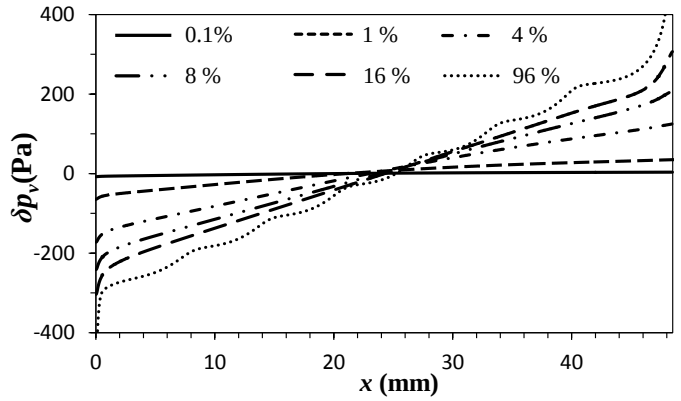

FIGURE 5. The spatial profile of the partial pressure of vapor for different average concentrations and $\Delta T = 10$ K. To amplify the variation of p_v in the central region of the cell we plotted the variation $\delta p_v = p_v - \langle p_v \rangle_x$ about the average and truncated the y-axis.

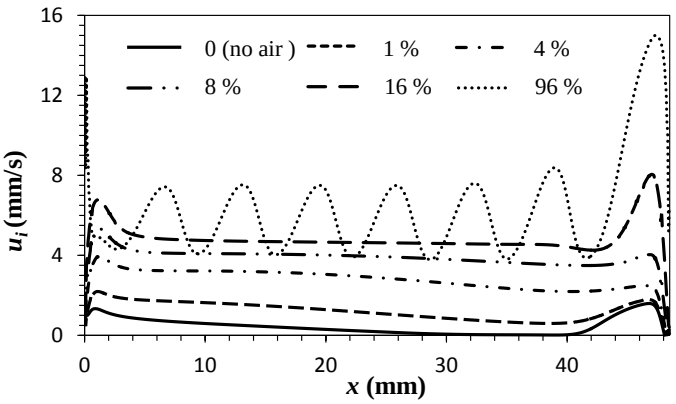

FIGURE 6. Interfacial velocity for different average concentrations of air and $\Delta T = 10$ K.

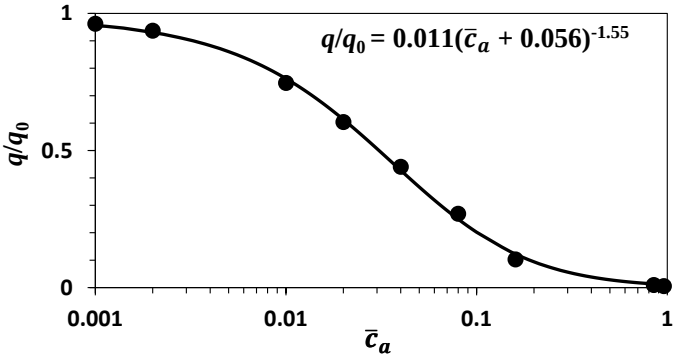

FIGURE 7. Effective heat flux, q normalized by its maximum value q_0 at $\bar{c}_a = 0$, as a function of the average concentration of air at $\Delta T = 10$ K. The dependence can be fitted with high accuracy ($R^2 = 0.9988$) by a simple power law.

than that at ambient conditions. This is in qualitative agreement with experiments [1], which find that the interfacial velocity at $\bar{c}_a = 0.11$ is almost the same as that at $\bar{c}_a = 0.96$. The slight increase in the flow velocity observed in experiments is likely due to the dependence of the temperature coefficient of surface tension γ on the composition of the gas phase, which has not been characterized for the silicone oil considered here.

Also similar to the experiments [1], we find that the interfacial flow is most sensitive to the concentration of noncondensables near the hot end wall, with the flow velocity decreasing noticeably as $\bar{c}_a$ is reduced from 96% to 8%. A further decrease in $\bar{c}_a$ should, based on these simulations, lead to a rather substantial drop in the flow velocity in the core region (where thermocapillarity dominates). In contrast, the flow near the hot wall (where buoyancy dominates) becomes essentially independent of $\bar{c}_a$ in the vapor-dominated limit. The flow near the cold end wall (where buoyancy is weaker than near the hot wall) is found to depend on $\bar{c}_a$ even at rather low concentrations, similar to the flow in the core region.

In the absence of air, the velocity profile has two local maxima: one near the hot end wall, and one near the cold end wall. These correspond to the two large convection rolls seen in Figure 2. Since both the interfacial temperature gradient and thermocapillary stresses are negligible in this limit, the flow is driven entirely by buoyancy which is most significant near the end walls. The flow velocity becomes very small in the region where the two convection rolls meet (28 mm $\lesssim x \lesssim$ 40 mm). Given that buoyancy should be independent of $\bar{c}_a$, any increase in the interfacial velocity beyond that at $\bar{c}_a = 0$ must be due to thermocapillarity. Surprisingly, these results show that small changes in $\bar{c}_a$ (between 0% and 4%) result in major and fundamental changes in the nature of thermocapillary-buoyancy convection. Specifically, the flow rapidly changes from one dominated by buoyancy in the absence of air to one dominated by thermocapillarity at $\bar{c}_a = 0.04$.

In terms of applications, it is useful to consider how the noncondensables affect the phase change and the associated heat flux. Assuming that the major limit on thermal performance for evaporative cooling devices is the rate at which heat is rejected by (*vs.* the transport of heat within) the device, the heat flux due to condensation can be estimated from the net mass flux over a thin layer next to the cold wall. For an arbitrarily defined region $0 < y < 2d_l$, the latent heat flux due to condensation is given by

$$q = \mathscr{L} W \int_0^{2d_l} J \sqrt{1 + (dz/dx)^2}\, dx. \tag{28}$$

Figure 7 shows how q, which is typically the most significant term in the overall heat flux of two-phase thermal management devices, changes as a function of $\bar{c}_a$. We find that a very small amount of noncondensables can make a large difference in heat flux. Introducing just 1% of noncondensables into the cell leads to a reduction of more than 20% in the heat flux, while 5% of noncondensables reduces the heat flux by more than 50%, compared with the maximum value q_0 at $\bar{c}_a = 0$.

CONCLUSIONS

We have developed, implemented, and validated a comprehensive numerical model of two-phase flows of confined volatile fluids, which accounts for momentum, mass, and heat transport in both phases and phase change at the interface. This model was used to investigate how the presence of noncondensable gases such as air affects buoyancy-thermocapillary convection in a layer of volatile liquid confined inside a sealed cavity subject to a horizontal temperature gradient.

The presence of air was found, as expected, to have a profound effect on the heat and mass transfer. The numerical results show that the flow in the liquid layer changes significantly as

the concentration of air in the gas layer is varied. Surprisingly, the average flow speed is found to be effectively independent of the average concentration of air over most of the free surface, from ambient conditions down to about 8%. The concentration of noncondensables does affect the flow under the free surface, however. Convection rolls that are present near the hot wall at ambient conditions weaken and disappear completely when the concentration of air is decreased to 16%.

The interfacial temperature profile is found to be determined by the concentration profile in the gas phase and both profiles are found to remain linear down to average concentrations of air as low as 2%, which explains why the flow profile and interfacial velocity remain uniform in the core region over a large range of parameters and conditions. The gradients in the interfacial temperature, and hence the thermocapillary stresses that typically dominate the flow, only disappear when the average concentration of noncondensables becomes extremely small (well below 1%).

ACKNOWLEDGMENT

This work has been supported by ONR under Grant No. N00014-09-1-0298. We are grateful to Zeljko Tukovic and Hrvoje Jasak for help with numerical implementation using OpenFOAM.

Nomenclature

α	Thermal Diffusivity
β	Coefficient of Thermal Expansion
γ	Temperature Coefficient of Surface Tension
μ	Dynamic Viscosity
ρ	Density
κ	Interfacial Curvature
σ	Surface Tension
λ	Accommodation Coefficient
τ	Interfacial Temperature Gradient
Σ	Stress Tensor
Bo_D	Dynamic Bond Number
c	Mole Fraction
$\bar{c}$	Average Mole Fraction
c_p	Heat Capacity
D	Binary Mass Diffusion Coefficient
d_l	Liquid Layer Thickness
m	Mass
M	Molar Mass
Ma	Marangoni Number
p	Pressure
p_0	Pressure Offset
Pr	Prandtl Number
R	Universal Gas Constant
$\bar{R}$	Specific Gas Constant
Ra	Rayleigh Number
t	Time
T	Temperature
T_0	Ambient Temperature
ΔT	Applied Temperature Difference
$\mathbf{u}$	Velocity
V	Volume
x, y, z	Coordinate Axes
g	Gravitational Acceleration
h_w	Wall Thickness
J	Mass Flux Across the Liquid-Gas Interface
k	Thermal Conductivity
$\mathscr{L}$	Latent Heat of Vaporization
L, W, H	Test Cell Dimensions

Superscript

$*$	Reference Value

Subscript

l	Liquid Phase
g	Gas Phase
v	Vapor Component
a	Air Component
i	Liquid-Gas Interface
s	Saturation
c	Cold End
h	Hot End

REFERENCES

[1] Li, Y., Grigoriev, R. O., and Yoda, M., 2014. "Experimental study of the effect of noncondensables on buoyancy-thermocapillary convection in a volatile low-viscosity silicone oil". *Phys. Fluids*. under consideration.

[2] Faghri, A., 1995. *Heat Pipe Science And Technology*. Taylor & Francis Group, Boca Raton.

[3] Qin, T., Željko Tuković, and Grigoriev, R. O., 2014. "Buoyancy-thermocapillary convection of volatile fluids under atmospheric conditions". *Int. J Heat Mass Transf.,* ***75***, pp. 284–301.

[4] Smith, M. K., and Davis, S. H., 1983. "Instabilities of dynamic thermocapillary liquid layers. part 1. convective instabilities". *J. Fluid Mech.,* ***132***, pp. 119–144.

[5] Smith, M. K., and Davis, S. H., 1983. "Instabilities of dynamic thermocapillary liquid layers. part 2. surface-wave instabilities". *J. Fluid Mech.,* ***132***, pp. 145–162.

[6] Villers, D., and Platten, J. K., 1992. "Coupled buoyancy and marangoni convection in acetone: experiments and comparison with numerical simulations". *J. Fluid Mech.,* ***234***, pp. 487–510.

[7] De Saedeleer, C., Garcimartín, A., Chavepeyer, G., Platten,

J. K., and Lebon, G., 1996. "The instability of a liquid layer heated from the side when the upper surface is open to air". *Phys. Fluids,* ***8***(3), pp. 670–676.

[8] Garcimartín, A., Mukolobwiez, N., and Daviaud, F., 1997. "Origin of waves in surface-tension-driven convection". *Phys. Rev. E,* ***56***(2), pp. 1699–1705.

[9] Riley, R. J., and Neitzel, G. P., 1998. "Instability of thermocapillarybuoyancy convection in shallow layers. Part 1. Characterization of steady and oscillatory instabilities". *J. Fluid Mech.,* ***359***, pp. 143–164.

[10] Ben Hadid, H., and Roux, B., 1992. "Buoyancy- and thermocapillary-driven flows in differentially heated cavities for low-prandtl-number fluids". *J. Fluid Mech.,* ***235***, pp. 1–36.

[11] Mundrane, M., and Zebib, A., 1994. "Oscillatory buoyant thermocapillary flow". *Phys. Fluids,* ***6***(10), pp. 3294–3306.

[12] Lu, X., and Zhuang, L., 1998. "Numerical study of buoyancy- and thermocapillary-driven flows in a cavity". *Acta Mech Sinica (English Series),* ***14***(2), pp. 130–138.

[13] Shevtsova, V. M., Nepomnyashchy, A. A., and Legros, J. C., 2003. "Thermocapillary-buoyancy convection in a shallow cavity heated from the side". *Phys. Rev. E,* ***67***, p. 066308.

[14] Zhang, J., Watson, S. J., and Wong, H., 2007. "Fluid flow and heat transfer in a dual-wet micro heat pipe". *J. Fluid Mech.,* ***589***, pp. 1–31.

[15] Kuznetzov, G. V., and Sitnikov, A. E., 2002. "Numerical modeling of heat and mass transfer in a low-temperature heat pipe". *J. Eng. Phys. Thermophys.,* ***75***, pp. 840–848.

[16] Kaya, T., and Goldak, J., 2007. "Three-dimensional numerical analysis of heat and mass transfer in heat pipes". *Heat Mass Transfer,* ***43***, pp. 775–785.

[17] Kafeel, K., and Turan, A., 2013. "Axi-symmetric simulation of a two phase vertical thermosyphon using eulerian two-fluid methodology". *Heat Mass Transfer,* ***49***, pp. 1089–1099.

[18] Fadhl, B., Wrobel, L. C., and Jouhara, H., 2013. "Numerical modelling of the temperature distribution in a two-phase closed thermosyphon". *Applied Thermal Engineering,* ***60***, pp. 122–131.

[19]

[20] Qin, T., and Grigoriev, R. O., 2012. "Convection, evaporation, and condensation of simple and binary fluids in confined geometries". In Proc. of the 3rd Micro/Nanoscale Heat & Mass Transfer International Conference, pp. paper MNHMT2012–75266.

[21] Qin, T., and Grigoriev, R. O., 2014. "The effect of noncondensables on buoyancy-thermocapillary convection in confined and volatile fluids". In Proc. of 11th AIAA/ASME Joint Thermophysics and Heat Transfer Conference, AIAA Aviation and Aeronautics Forum and Exposition, pp. paper AIAA2014–1898558.

[22] Schrage, R. W., 1953. *A Theoretical Study of Interface Mass Transfer*. Columbia University Press, New York.

[23] Wayner, P. J., Kao, Y. K., and LaCroix, L. V., 1976. "The interline heat transfer coefficient of an evaporating wetting film". *Int. J. Heat Mass Transfer,* ***19***, pp. 487–492.

[24] Wang, H., Pan, Z., and Garimella, S. V., 2011. "Numerical investigation of heat and mass transfer from an evaporating meniscus in a heated open groove". *Int. J. Heat Mass Transfer,* ***54***, p. 30153023.

[25] `http://www.openfoam.com`.

[26] Yaws, C. L., 2003. *Yaws' Handbook of Thermodynamic and Physical Properties of Chemical Compounds (Electronic Edition): physical, thermodynamic and transport properties for 5,000 organic chemical compounds*. Knovel, Norwich.

[27] Yaws, C. L., 2009. *Yaws' Thermophysical Properties of Chemicals and Hydrocarbons (Electronic Edition)*. Knovel, Norwich.